TU Delft

Delft University of Technology

Coupling model of electromigration and experimental verification – Part II
Impact of thermomigration

Cui, Zhen; Fan, Xuejun; Zhang, Yaqian; Vollebregt, Sten; Fan, Jiajie; Zhang, Guoqi

DOI
10.1016/j.jmps.2023.105256

Publication date
2023

Document Version
Final published version

Published in
Journal of the Mechanics and Physics of Solids

Citation (APA)
Cui, Z., Fan, X., Zhang, Y., Vollebregt, S., Fan, J., & Zhang, G. (2023). Coupling model of electromigration and experimental verification – Part II: Impact of thermomigration. *Journal of the Mechanics and Physics of Solids*, *174*, Article 105256. https://doi.org/10.1016/j.jmps.2023.105256

Important note
To cite this publication, please use the final published version (if applicable).
Please check the document version above.

Copyright
Other than for strictly personal use, it is not permitted to download, forward or distribute the text or part of it, without the consent of the author(s) and/or copyright holder(s), unless the work is under an open content license such as Creative Commons.

Takedown policy
Please contact us and provide details if you believe this document breaches copyrights.
We will remove access to the work immediately and investigate your claim.

This work is downloaded from Delft University of Technology.
For technical reasons the number of authors shown on this cover page is limited to a maximum of 10.

J. Mech. Phys. Solids 174 (2023) 105256

Contents lists available at ScienceDirect

Journal of the Mechanics and Physics of Solids

journal homepage: www.elsevier.com/locate/jmps

Coupling model of electromigration and experimental verification – Part II: Impact of thermomigration

Zhen Cui [a], Xuejun Fan [b,a,*], Yaqian Zhang [a], Sten Vollebregt [a], Jiajie Fan [c], Guoqi Zhang [a,*]

[a] Department of Microelectronics, Delft University of Technology, 2628 CD, Delft, the Netherlands
[b] Department of Mechanical Engineering, P.O. Box 10028, Lamar University, Beaumont, TX 77710, USA
[c] Academy for Engineering & Technology, Fudan University, Shanghai, 200433, PR China

ARTICLE INFO

Keywords:
Thermomigration
Electromigration
SWEAT structure
Joule heating
Temperature gradient
Threshold product
Acceleration factor

ABSTRACT

This paper presented a comprehensive experimental and simulation study for thermomigration (TM) accompanying electromigration (EM) at elevated current densities. Both Blech and standard wafer-level electromigration acceleration test (SWEAT)-like test structures, with aluminum (Al) as a carrier, were used for testing and analysis. In Part I of our study (Cui et al., 2023a), the experimental and numerical results with the current density of 1 MA/cm^2 were presented. We observed that Al stripes with a SWEAT structure did not show damage in the entire length, while Blech structures showed void and hillock formations only at the cathode and anode, respectively. The temperature gradient owing to Joule heating was neglected in our previous simulations, and the predicted results agreed well with the experimental observations. However, we have not theoretically verified the effect of the temperature gradient. In this paper, we first reported the new experimental data under the elevated current densities of 3 and 5 MA/cm^2. In both Blech and SWEAT structures, the spreading of voids in the middle region of conductors was observed. Moreover, in Blech structures, voiding in the middle region occurred after a period of time when voids/hillocks were formed at the cathode and anode, while the SWEAT structures did not show damage at the two ends. Next, based on the coupled 3D theory (Cui et al., 2023a), new analytical one-dimensional (1D) solutions were derived for the Blech and SWEAT structures in the un-passivated configuration considering TM. We found that TM played a significant role in the EM development in the middle of conductors under the elevated current density. The numerical results were in excellent agreement with the experimental data with the consideration of TM. We further established new EM failure's threshold criteria for the SWEAT structures in the form of the product of current density and square of conductor length. This is a major departure from the original Blech's theory in which only mechanical stress gradient was considered. We also studied the acceleration factor of the current density exponent and presented an insight into failure mechanisms associated with TM.

1. Introduction

Thermomigration (TM) is a mass transport driven by a temperature gradient. This effect is called Soret effect (also known as

* Corresponding author.
E-mail addresses: xuejun.fan@lamar.edu (X. Fan), g.q.zhang@tudelft.nl (G. Zhang).

https://doi.org/10.1016/j.jmps.2023.105256
Received 23 November 2022; Received in revised form 13 February 2023; Accepted 27 February 2023
Available online 4 March 2023
0022-5096/© 2023 The Author(s). Published by Elsevier Ltd. This is an open access article under the CC BY-NC-ND license (http://creativecommons.org/licenses/by-nc-nd/4.0/).

Ludwig–Soret effect) in fluids (Ludwig, 1856; Platten, 2006; Rahman and Saghir, 2014). Similar to thermoelectric effects, in which a temperature gradient can drive electrons, a temperature gradient can also drive atomic transport in solids. TMs have been studied since 1856 and are found in pure metals such as Al, Au, Cu, and In (Christou, 1973; Meechan and Lehman, 1962; Oriani, 1969; Swalin and Yin, 1967; Van Gurp et al., 1985). In addition, when an inhomogeneous binary alloy is subjected to a temperature gradient, it may become homogenous. On the other hand, a homogeneous binary alloy, when subjected to a temperature gradient, may become inhomogeneous due to TM (Chen et al., 2012a; Piazza and Guarino, 2002).

Electromigration (EM) is inevitably accompanied by TM (Chen et al., 2010; Hemmert and Costa, 1991; Lloyd, 1999; Tu et al., 2017). When a high electrical current is applied to a microelectronic device, Joule heating induces temperature gradients. While EM is an enhanced mass transport process due to momentum transfer between conducting electrons and diffusing metal atoms driven by current density, TM, self-diffusion due to atomic concentration gradient, and stress migration due to hydrostatic stress gradient, are coupled with each other (Cui, 2021; Cui et al., 2019; Kijkanjanapaiboon, 2017). As shown in Eq. (1), the total atomic flux, $\boldsymbol{J}_a$, during EM, is generally written as follows.

$$\boldsymbol{J}_a = D_a\left(- C_a\frac{Z^* e\rho \boldsymbol{j}}{k_B T} - \nabla C_a + C_a\frac{\Omega\nabla\sigma}{k_B T} - C_a\frac{Q^*\nabla T}{k_B T^2}\right) \tag{1}$$

where C_a is the atomic concentration, D_a is the atomic diffusivity(m^2/s), Z^* is the effective charge number ($Z^*>0$), e is the elementary charge, ρ is the electrical resistivity, $\boldsymbol{j}$ is the current density vector, k_B is the Boltzmann constant, Ω is the volume per atom, T is the temperature, σ is the hydrostatic stress, and Q^* is the heat of transport. Eq. (1) contains all driving/resistive fluxes for atomic transport, namely, the diffusional terms by the atomic concentration gradient, the EM itself, the stress migration, and the TM, respectively.

In the first part of our study (Cui et al., 2023a), we experimentally observed, under the current density of 1 MA/cm^2, that Al stripes with a SWEAT structure did not show damage in the entire conductor's length, while Blech structure showed void and hillock formations only at the cathode and anode, respectively. Consequently, the temperature gradient owing to Joule heating, i.e., the last term on the right side of Eq. (1), was neglected in our previous simulations. The simulation results agreed well with the experimental observations. However, we have not theoretically verified the effect of temperature gradient on EM development.

As Joule heating is squarely proportional to the magnitude of current density, it is important to review the range of current density used in various accelerated EM tests in the literature. Two test structures are commonly used: Blech and standard wafer-level electromigration acceleration test (SWEAT) or SWEAT-like structures (Tan and Roy, 2007; Tu, 2003). Blech structure refers to a test structure in which both ends of a metal line segment are in perfectly blocking conditions, allowing no atomic flux (Blech and Herring, 1976; Blech and Meieran, 1969; Blech, 1976). In line-via test structures (Hu and Luther, 1995; Hu et al., 1992, 1993; Liu, 2017), individual metal line segments may be considered as Blech-like structures owing to the barrier or capping layer at the via/line interface. Blech structures were mainly used to investigate the threshold condition for EM-induced damage. Thus the applied current density was at a relatively moderate level ranging from 0.1 to 1.0 MA/cm^2 for Al (Blech and Meieran, 1969; Blech, 1976; Nucci et al., 2002; Proost et al., 2002, 1998; Ross et al., 1989). On the other hand, SWEAT or SWEAT-like structures refer to the metal line connected to large pads at the ends (Giroux et al., 1995, 1994; Jeong et al., 2014; Kozlova et al., 2013). Large current densities and long lengths were often applied with SWEAT structures in Al, ranging from 2 to 30 MA/cm^2 (d'Heurle, 1971; Giroux et al., 1995; Kraft et al., 1997; Lee et al., 2001). Different from Blech structures, in SWEAT structures, voids were observed either near the center of the metal conductor or spreading in a wide range of center regions (Giroux et al., 1995; Lee et al., 2001). Additionally, it took longer (about 200 h) to observe failure at the current density of 2 MA/cm^2 in Al with a SWEAT structure (d'Heurle, 1971). Although the atomic divergence due to different atomic diffusivity caused by temperature gradients was thought to be responsible for EM failure, it is not clear how TM affects EM when the current density increases.

Blech and SWEAT test structures were also used for other metal lines, such as Cu and Au, subjected to a wide range of current densities from 0.5 to 10 MA/cm^2 (Lee et al., 1995; Liang et al., 2020a, b; Somaiah and Kumar, 2018; Stahlmecke and Dumpich, 2007). Somaiah *et al.* (Somaiah and Kumar, 2018) reported EM/TM coupling in Cu/W Blech structures under a current density of 4 MA/cm^2, indicating void and hillock formations only at the cathode and anode. Lee *et al.* (Lee et al., 1995) investigated the EM failure in Cu with a Blech structure under a current density from 0.5 to 2 MA/cm^2, in which only the void and hillock formation at the cathode and anode was reported. Liang *et al.* (Liang et al., 2020a, b) studied EM failure in Cu redistribution lines (RDL) at a current density of 6 MA/cm^2, showing void formations at the center of the line. No studies, however, have been reported using both Blech and SWEAT structures to examine the underlying EM/TM failure mechanism under the elevated current density.

Tu pioneered the EM studies in solder joints in flip-chip assemblies (Chen et al., 2012b, 2010, 2008; Huang et al., 2006; Shen et al., 2019; Tu et al., 2017). He pointed out that despite an average current density in a range of 10^4 A/cm^2 (0.01 MA/cm^2) in solder bumps, EM did occur in bumps. Furthermore, Chen *et al.* (Chen et al., 2008) designed a test structure consisting of several micro-bumps, in which some of which were unpowered. Through the externally Joule heated chip on the top of solder bumps, the temperature gradient existed for both powered and unpowered solder bumps. They demonstrated that TM became an independent factor from the EM, as the unpowered solder bump had damage under the temperature gradient only. They found if there is a temperature difference of 1 °C across a micro-bump of 10 μm, the temperature gradient would be 1000 °C/cm, which can cause TM at the device operating temperature of around 100 °C. Additionally, they observed that in Pb-free SnAg solder bumps, the Sn atoms moved to the hot end, but the Ag atoms migrated to the cold end (Hsiao and Chen, 2009). Moreover, the TMs of other metallization elements, such as Cu (Abdulhamid et al., 2009; Chen et al., 2008), Ti (Chen et al., 2012c), and Ni (Cahn and Haasen, 1996), were also observed in solder bumps. Cu diffused rapidly interstitially to the cold end, forming voids in the hot end. It is interesting noting that Q^*, the heat of transport in Eq. (1), can be positive or negative, which determines the direction of TM for different species (Chen et al., 2012b; Oriani, 1969).

Various theories and models describing EM have been developed. The early models (He et al., 2004; Kirchheim, 1992; Korhonen et al., 1993; Sarychev et al., 1999), including Blech's theory (Blech and Herring, 1976; Blech, 1976), were mainly devoted to investigate the mechanical stress effect during EM. Additionally, Ceric *et al.* (Ceric et al., 2008, 2006) and Zhang *et al.* (Zhang et al., 2012) used sequentially coupled finite element analysis, but without considering the coupling of diffusion-induced strain, to investigate the time-to-failure in chips and solder bumps, respectively. Basaran and his group performed a series of studies to investigate the interactions between TM and EM, primarily focusing on solder joints (Abdulhamid et al., 2009; Yao and Basaran, 2013; Ye et al., 2003). They reported the combined effect of TM and EM in solder joints, indicating that TM may assist or counteract EM depending on the thermal gradient direction. Sukharev et al. (Sukharev and Zschech, 2004; Sukharev et al., 2007) established a 3D coupling model but neglected the Joule heating effect and TM in the case studies.

Most accelerated EM tests in the literature mentioned above used low to moderate levels of current density in Blech structures, while using SWEAT-like structures, moderate to high levels of current density were applied to generate the failure located in the center of the conductor. In this paper, the TM accompanying EM was investigated through integrated studies of experiment, theory, and simulation. First, EM test specimens with different geometries and structures were tested under elevated current densities and extended time durations. Both Blech and SWEAT structures were applied and tested for comparison. Tapered and two-dimensional (2D) shapes of conductors were used. Second, by considering self-Joule heating, one-dimensional (1D) temperature distribution and its gradient were obtained. Furthermore, temperature gradient-induced flux and temperature-dependent diffusivity were taken into consideration. Moreover, based on the coupled 3D theory (Cui et al., 2023a), new analytical 1D governing equations were derived for the Blech and SWEAT structures in the un-passivated configuration considering TM. The numerically predicted results were then compared extensively with the experimental data under various current densities. Furthermore, with the consideration of TM, the threshold condition for EM failure was reexamined. The current density exponent *n*, introduced by Black, was also revisited by taking TM into consideration. Finally, we presented conclusions and outlooks.

2. Experiment

As described in (Cui et al., 2023a), EM test specimens were fabricated on 4-inch silicon wafers. A full EM test wafer consisted of 52 dies, each having 63 test specimens. Fig. 1 illustrated the schematic of the cross-section of the layer stack (Fig. 1(a)) and the geometry of test specimens used in this study. Two geometries of Blech structures were used: one with three lengths of 30/60/100 μm on a stripe and one with a single length of 800 μm, as shown in Fig. 1(b). In SWEAT structures, three different geometries were used: a single length of 800 μm, a tapered shape containing four segments with varying widths of 3/6/12/15 μm but the same length of 100 μm, and a 2D shape in which each horizontal and vertical segment was 150 μm and 50 μm, respectively (Fig. 1(c)). The Al thickness of all specimens was 200 nm, and the width was 5 μm except for the tapered specimens.

We previously reported the experimental results only under the current density of 1 MA/cm^2 (Cui et al., 2023a). In order to explore the effects of Joule heating, the current densities of 1, 3, and 5 MA/cm^2 were applied in this study. All measurements were performed in a vacuum condition, and the ambient temperature was 250 °C. In the literature, the commonly used ambient temperature in EM acceleration tests was from 200 to 350 °C (Tan and Roy, 2007). Al specimens without annealing and passivation were used in this study. Each specimen was removed from the test chamber at various time intervals during the test for optical measurement using a laser scanning microscope. Each geometry was tested multiple times for repeatability and consistency checks.

2.1. Blech structure

Three current densities of 1 MA/cm^2, 3 MA/cm^2, and 5 MA/cm^2 were applied to 800 μm length specimens first. Fig. 2 showed the

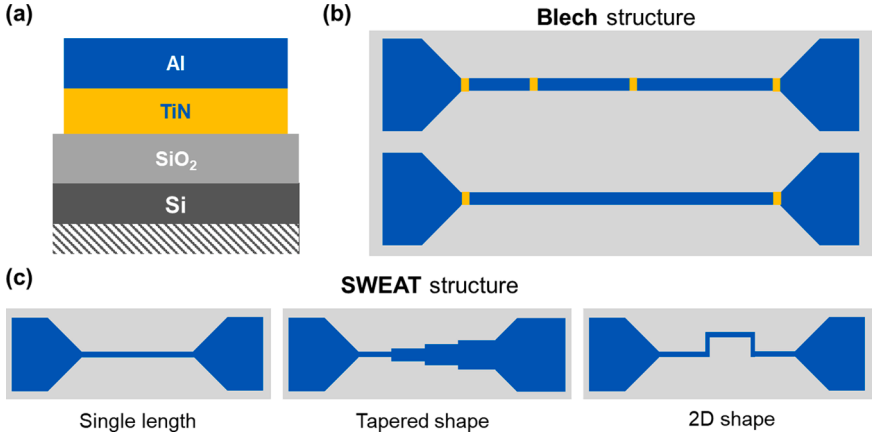

Fig. 1. Schematic of the cross-section and the geometry of EM test specimens (a) wafer's cross-section, (b) geometries of Blech structures, (c) geometries of a single-length, a tapered-shape, and a 2D-shape SWEAT structures.

optical images at various time intervals under different current densities j. As expected, voids were formed and grown at the cathode side, and hillocks were formed and grown near the anode side with time progressing. Under $j = 1$ MA/cm^2, no voids and hillocks were observed in the middle regions of the conductors, even at 20 h, as shown in Fig. 2(a). When j was increased to 3 MA/cm^2, still no damage in the middle of the specimen was found until 3 h. However, the voids in the middle region were observed at 5 h, as shown in Fig 2(b). Previously, we observed that void formed at the cathode as early as 30 min under $j = 1$ MA/cm^2 (Cui et al., 2023a). This implied that there was a significant time lag between the voids formed at the cathode and in the middle under $j = 3$ MA/cm^2. Also shown in Fig. 2(b), voids were seen in a wide range of middle regions in the conductor at 20 h. With further increasing j to 5 MA/cm^2, we observed void formation in the middle region as early as 20 min, as shown in Fig. 2(c). At 5 h, a cut-through void near the center region was observed, indicating the breaking of the conductor.

To our knowledge, no study in the literature reported the growth of voids in the middle region of conductors with Blech structures. One reason may be that the Blech structure was mainly used to study the critical current density and/or conductor length. Therefore, the applied current density was at a relatively moderate level (Blech and Tai, 1977; Blech, 1976; Proost et al., 2002, 1998). Another reason is that there is a time delay between the formation of voids in the middle region and the formation at the cathode. Most tests were stopped when voids were observed at the cathode. Additionally, we used 800 μm length specimens. Such a length was suggested and primarily used in SWEAT structures (Schafft et al., 1987). The damage in the middle region of specimens was caused by TM due to self-Joule heating (to be discussed in Section 4). The maximum temperature gradient under each current density, as shown in Fig. 2, was obtained from a theoretical solution presented in the next section. The maximum temperature gradient was 144 K/cm, 1296 K/cm, and 3600 K/cm when j was 1, 3, and 5 MA/cm^2, respectively.

To further investigate the effect of Joule heating in Blech structures, we tested different lengths under $j = 3$ MA/cm^2. Fig. 3 showed the optical images of Al specimens of 60 μm, 100 μm, and 800 μm lengths at 20 h. No damage in the middle regions of the conductors was observed for the lengths of 60 μm and 100 μm at 20 h. The maximum temperature gradient, as shown in the figure, was 97 K/cm, 162 K/cm, and 1296 K/cm when the conductor length was 60 μm, 100 μm, and 800 μm, respectively. This indicated that the temperature gradient is also dependent on the conductor length.

One of the explanations in the literature for the void formation in a broad range of conductors was the atomic flux divergence at grain-boundary triple points (Berenbaum, 1971; Shen et al., 2021; Tan and Roy, 2007). If we assume that triple points could affect the EM damage, voids formation will occur regardless of the conductor length. However, the present experimental results shown in Fig. 3 showed that under the same current density and testing time, the void formation in the middle of the conductor only occurred at the 800 μm Al line. There were no signs of void formations in the middle region of 60 and 100 μm Al lines.

2.2. SWEAT structure

The specimens with a single-length stripe of 800 μm were tested first. Fig. 4 showed the optical images at various time intervals under different current densities j and the corresponding in-situ electrical resistance. There was no damage observed in the entire

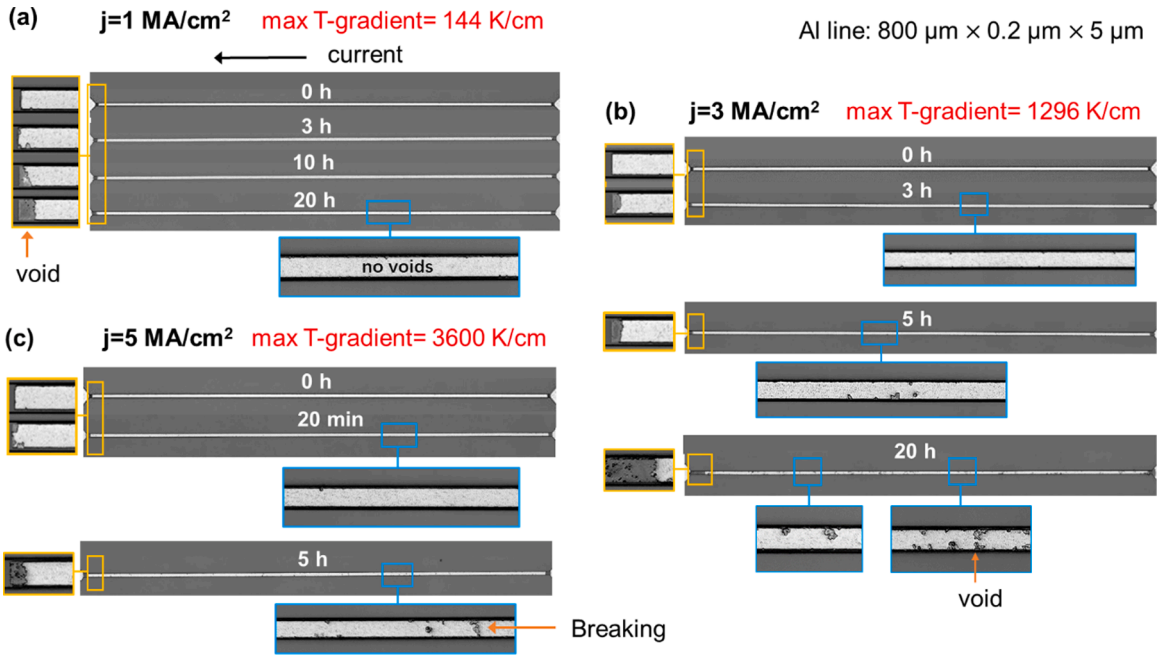

Fig. 2. Optical images of 800 μm length specimens with Blech structure at various time intervals under different current densities. The electrical current flowed from right to left. (a) $j = 1$ MA/cm^2. (b) $j = 3$ MA/cm^2. (c) $j = 5$ MA/cm^2.

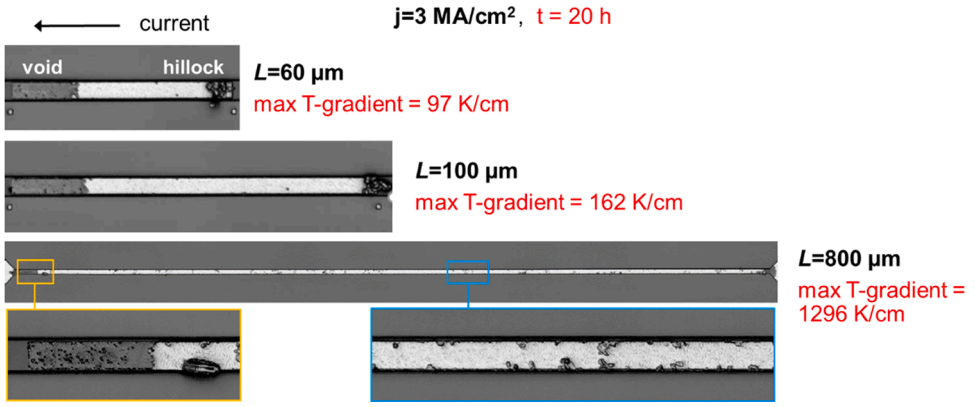

Fig. 3. Optical microscope images for 60/100/800 μm lengths Al lines with Blech structure were under the current density of 3 MA/cm^2 and temperature of 250 °C at 20 h.

length of the SWEAT structures when $j = 1$ MA/cm^2, as shown in Fig. 4(a). When j was increased to 3 MA/cm^2, in Fig. 4(b), however, several small voids were observed in a broad middle region at 5 h, then large voids were observed at 16 h. Finally, the conductor broke to the right of the center at 20 h. Unlike the damage at both ends in the Blech structure, which occurred at a very early stage, the void formation in the SWEAT structures occurred later and only in the middle of the conductor. When j further increased to 5 MA/cm^2, voids spread over a wide range of the conductor, breaking to the right of the center at 5 h. The maximum temperature gradient was also shown in Fig. 4(a) to (c) under each current density. Futhermore, in Fig. 4(d), the electrical resistance as a function of time was plotted under different current densities. The resistance changed slightly under $j = 1$ MA/cm^2, indicating no or negligible EM damage. Under the elevated current density, however, there was a region with a rapid change in the slope of the resistance curve, indicating the breaking of the conductor.

To further investigate the effect of Joule heating, tapered-shaped specimens were tested, as shown in Fig. 5. The current density in the four segments was 1 MA/cm^2, 1.25 MA/cm^2, 2.25 MA/cm^2, and 5 MA/cm^2 from the right. We tested the current flows in two directions: right-to-left (Fig. 5(a)), and left-to-right (Fig. 5(b)). In both cases, no failures were found at 5 h for the segment with $j = 1$ MA/cm^2, 1.25 MA/cm^2, and 2.25 MA/cm^2. However, significant damages were observed in the narrowest segment with $j = 5$ MA/cm^2 at 5 h. The results clearly demonstrated the importance of current density in SWEAT structures. Moreover, when the current flowed from right to left, the conductor broke slightly to the right of the center. On the other hand, when the current flowed from left to right, the conductor broke slightly to the left of the center. Additionally, current crowding occurred at the junctions of discontinuity of cross-

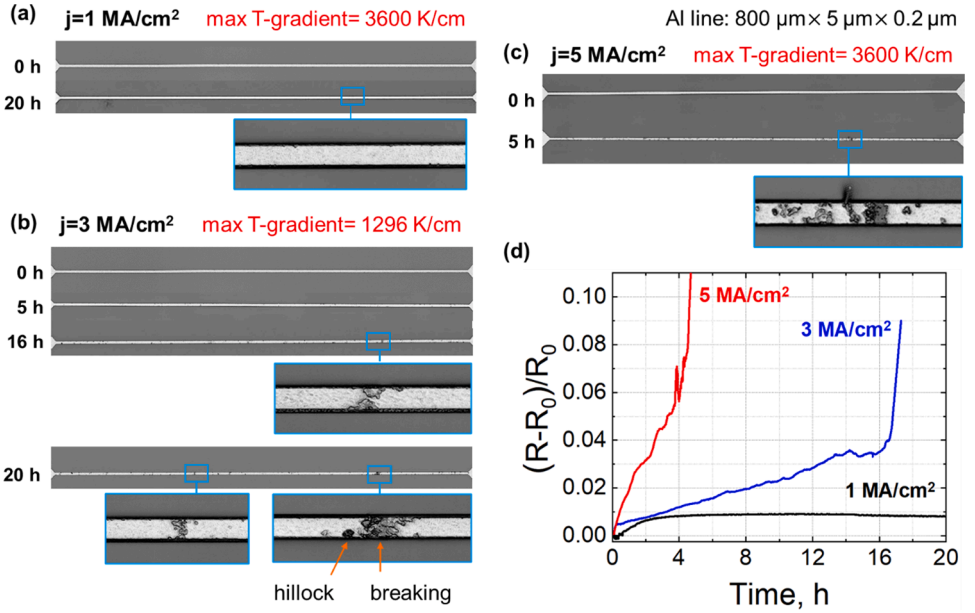

Fig. 4. Optical microscope images of 800 μm-length Al lines with SWEAT structure at various time intervals under different current densities at the temperature of 250 °C. The electrical current flowed from right to left. (a) $j = 1$ MA/cm^2, (b) $j = 3$ MA/cm^2, (c) $j = 5$ MA/cm^2, (d) in-situ electrical resistance change.

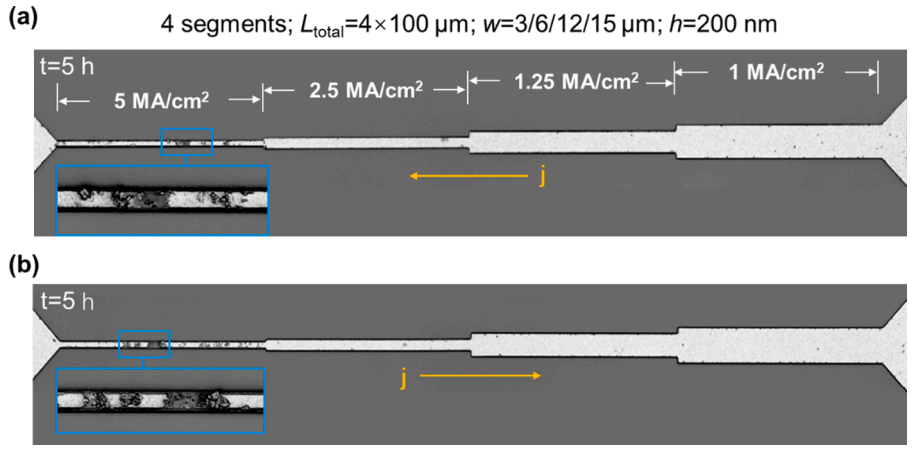

Fig. 5. Optical microscope images of the tapered shape of 400 μm-length Al line. (a) right-to-left current flow (b) left-to-right current flow.

section, but no damage was observed in those locations (Dandu and Fan, 2011).

Furthermore, the specimens with a 2D shape were tested under $j = 5$ MA/cm^2. Damages spread in each line segment at 5 h, as shown in Fig. 6. Current crowding occurred at corners, but no obvious voids were observed at these corners (Dandu and Fan, 2011).

In conclusion, for Blech structures, we observed damage not only at two ends but also spreading in a wide range of middle regions under the elevated current density. It appeared that the temperature gradient had a strong correlation with the failure in the middle regions. We also found that voids were developed in the middle regions at a later stage, while the voids and hillocks formed at the cathode and the anode occurred in an early stage. This implied that the effect of temperature gradient on atomic transport was slower than the effect due to electron wind. For the SWEAT structures, the voids spread in a wide range of the conductors but no damage at both ends when subjected to the elevated current density. Overall, the time to failure in SWEAT structures occurred at an approximately similar time interval compared to the middle-range voids in Blech structures. We again found a strong correlation between damage and temperature gradient in SWEAT structures. As described in many papers (Giroux et al., 1995, 1994; Kraft and Arzt, 1998), SWEAT structures were mainly used to study the Joule heating effect. Therefore, a long conductor's length, a high current density and a longer time were needed to observe the damage during EM (d'Heurle, 1971; Giroux et al., 1995, 1994; Kraft and Arzt, 1998).

3. Theory

We developed 1D analytical solutions in both un-passivated and passivated configurations without considering the effect of the temperature gradient, i.e., the last term on the right side of Eq. (1) (Cui et al., 2023a). Here, when all the terms of Eq. (1) are considered, the governing equation for atomic transport can be described by a mass conservation equation as follows (Cui et al., 2019; Tan and Roy, 2007),

$$\frac{\partial \theta}{\partial t} = -\Omega D_a \nabla \cdot \left(D_a^{-1} \boldsymbol{J}_a \right) \tag{2}$$

where θ is the total volumetric strain that generally consists of the strain due to mechanical deformation, thermal strain, and diffusion. As discussed in (Cui et al., 2019, 2020), Eq. (2) naturally includes the source/sink term to account for the formation and annihilation of vacancies. Because the total atomic flux ($\boldsymbol{J}_a$) and volumetric strain (θ) involve the deformation, current density, the gradients of hydrostatic stress, and temperature, Eq. (2) is coupled with electric, temperature, displacement-strain, and mechanical stress fields. When linear elasticity is assumed, stress and deformation equations are given as follows,

$$\theta = tr(\boldsymbol{\varepsilon}) \tag{3}$$

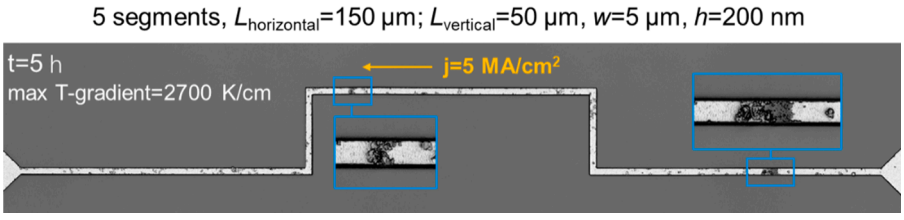

Fig. 6. Optical microscope image of the 2D shape Al conductor containing three horizontal segments with the length of 150 μm and two vertical segments with the length of 50 μm.

$$\boldsymbol{\varepsilon} = \boldsymbol{\varepsilon}^{\mathrm{me}} + \boldsymbol{\varepsilon}^{\mathrm{th}} + \boldsymbol{\varepsilon}^{\mathrm{diff}} \tag{4}$$

$$d\boldsymbol{\varepsilon}^{\mathrm{th}} = \alpha dT\boldsymbol{I} \tag{5}$$

$$\boldsymbol{\sigma} = \lambda tr(\boldsymbol{\varepsilon}^{\mathrm{me}})\boldsymbol{I} + 2G\boldsymbol{\varepsilon}^{\mathrm{me}} \tag{6}$$

$$\sigma = tr(\boldsymbol{\sigma})/3 \tag{7}$$

$$\nabla \cdot \boldsymbol{\sigma} + \boldsymbol{F} = 0 \tag{8}$$

$$\boldsymbol{\varepsilon} = \frac{1}{2}(\nabla \boldsymbol{u} + \boldsymbol{u}\nabla) \tag{9}$$

where $\boldsymbol{\varepsilon}$ is the total strain, $\boldsymbol{\varepsilon}^{\mathrm{me}}$ the elastic strain, $\boldsymbol{\varepsilon}^{\mathrm{th}}$ the thermal strain, $\boldsymbol{\varepsilon}^{\mathrm{diff}}$ is the diffusion-induced strain, α is the coefficient of thermal expansion, $\boldsymbol{I}$ is the unit tensor, G and λ are lamé constants $2G=E/(1+\nu)$ and $\lambda=2G\nu/(1-2\nu)$, E is the Young's modulus, ν is the Poisson's ratio, $\boldsymbol{F}$ is the body force (N), and $\boldsymbol{u}$ is the displacement (m).

For a substitutional diffusion, the diffusion-induced strain, $\boldsymbol{\varepsilon}^{\mathrm{diff}}$ in Eq. (4), can be described as follows (Cui et al., 2021),

$$d\theta^{\mathrm{diff}} = (1-f)\frac{dC_a}{C_a} \tag{10}$$

where f is the vacancy volume relaxation factor that varies between 0 and 1, i.e., $0 < f < 1$. The atomic concentration C_{a}, the displacement vector $\boldsymbol{u}$, and the stress tensor $\boldsymbol{\sigma}$, are coupled through the above equations. Additionally, the electrical and temperature fields are given as follows,

$$\nabla \cdot \boldsymbol{j} = 0 \tag{11}$$

$$\boldsymbol{j} = \frac{\boldsymbol{E}}{\rho} \tag{12}$$

$$k_T \nabla^2 T + \boldsymbol{j} \cdot \boldsymbol{E} = 0 \tag{13}$$

where $\boldsymbol{E}$ is the electric field (V/m), and k_T is the thermal conductivity ($\mathrm{W \bullet K^{-1}}$). Eqs. (11) – (13) are sequentially coupled with mechanical stress, deformation, and atomic concentration fields. This means that Eqs. (11) and (12) are solved first to obtain the electric current j. Then Eq. (13) is used to solve for temperature field T. Subsequently, Eqs. (1) to (10) are solved concurrently to obtain the final solution for atomic concentration C_a $(\boldsymbol{x},\ t)$ and stress field $\boldsymbol{\sigma}$.

According to the failure criterion described in (Cui et al., 2023a), an EM failure occurs when

$$C_{\mathrm{a}}(\boldsymbol{x}, t) = C_{\mathrm{a,critical}} \tag{14}$$

where $C_{\mathrm{a,critical}}$ is the critical atomic concentration. The time to failure, t_{failure}, and the failure location $\boldsymbol{x}$ can then be determined accordingly using Eq. (14).

Let us consider a one-dimensional (1D) problem where all field variables depend only on x and t, as shown in Fig. 7. When a constant current density j was applied along the negative direction of the conductor (i.e., $-j$), assuming that all stress components were zeros in the un-passivated conductor and the temperature reached steady state, the volumetric strain θ and the atomic flux J_a were simplified as follows,

$$\frac{\partial \theta}{\partial t} = \frac{\partial \theta^{\mathrm{diff}}}{\partial t} = \frac{1-f}{C_a}\frac{\partial C_a}{\partial t} \tag{15}$$

$$J_a = D_a\left[\frac{Z^* e\rho j C_a}{k_B T_{\mathrm{m}}} - \frac{\partial C_a}{\partial x} - \frac{Q^* C_a}{k_B T_{\mathrm{m}}^2}\frac{dT}{dx}\right] \tag{16}$$

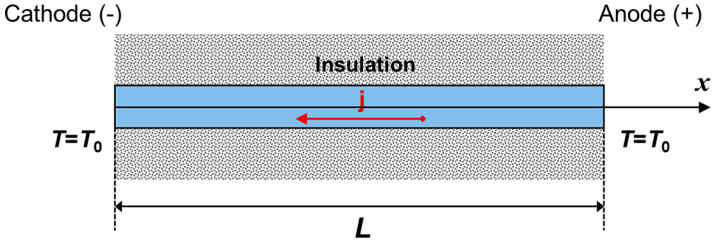

Fig. 7. Schematic of 1D EM problem where atomic concentration $C_{\mathrm{a}}(x,t)$ and hydrostatic stress $T(x)$ are the two unknowns.

Then, Eq. (2) was rewritten as follows,

$$\frac{1-f}{C_a}\frac{\partial C_a}{\partial t} = D_a\left[-\frac{Z^* e\rho j}{k_B T_{\mathrm{m}}}\frac{\partial C_a}{\partial x} + \frac{\partial^2 C_a}{\partial x^2} + \frac{Q^*}{k_B T_{\mathrm{m}}^2}\frac{\partial C_a}{\partial x}\frac{dT}{dx} + \frac{Q^* C_a}{k_B T_{\mathrm{m}}^2}\frac{d^2 T}{dx^2}\right] \tag{17}$$

where T_{m} is the average temperature along the conductor as follows,

$$T_{\mathrm{m}} = \frac{1}{L}\int_0^L T dx \tag{18}$$

Eq. (17) is a general 1D governing equation in un-passivated conductors for both Blech and SWEAT structures. In the steady state, Eq. (17) is reduced to an ordinary differential equation as follows,

$$0 = -\frac{Z^* e\rho j}{k_B T_{\mathrm{m}}}\frac{dC_a}{dx} + \frac{d^2 C_a}{dx^2} + \frac{Q^*}{k_B T_{\mathrm{m}}^2}\frac{dC_a}{dx}\frac{dT}{dx} + \frac{Q^* C_a}{k_B T_{\mathrm{m}}^2}\frac{d^2 T}{dx^2} \tag{19}$$

In both Eqs. (17) and (19), temperature field T is solved globally at a system level using Eq. (13), because a 1D conductor segment generally is a sub-part of the whole system. In the following, we considered self-Joule heating in a conductor shown in the experiments. We derived the solutions for temperature and the corresponding atomic concentration evolutions in both Blech and SWEAT structures.

3.1. Temperature distribution

Considering 1D heat conduction, Eq. (13) was rewritten as follows,

$$k_T\frac{d^2 T}{dx^2} + j^2\rho = 0 \tag{20}$$

where at both ends, temperature equals to the environment temperature T_0,

$$T(0) = T(L) = T_0 \tag{21}$$

The solutions for temperature and temperature gradient were then obtained as follows

$$T(x) = -\frac{j^2\rho}{2k_T}x^2 + \frac{j^2\rho L}{2k_T}x + T_0 \quad \left(T_{max} = \frac{j^2 L^2\rho}{8k_T} + T_0\right) \tag{22}$$

$$\frac{dT(x)}{dx} = -\frac{j^2\rho}{k_T}x + \frac{j^2\rho L}{2k_T} \quad \left(\left.\frac{dT}{dx}\right|_{max} = \frac{j^2\rho L}{2k_T}\right) \tag{23}$$

These equations showed that the maximum temperature is proportional to the square product of current density and conductor length (j^2L^2), and the maximum temperature gradient increases linearly with conductor length (L) and squarely with current density (j^2). Because the majority of the heat in our test setup was dissipated through a silicon substrate, to keep the Eq. (20) consistent with Eq. (13), a modified thermal conductivity was used as k_{T}=k_{Al}/(1-q), in which q is considered as a percentage of heat dissipated through the substrate (q = 0.9967) (Cui et al., 2023b).

3.2. Blech structure

Applying Eqs. (22) and (23) to Eq. (17), the governing equation of atomic concentration in an un-passivated conductor was obtained as follows,

$$\frac{1-f(C_a)}{C_a}\frac{\partial C_a}{\partial t} = D_a\left[-\frac{Z^* e\rho j}{k_B T_{\mathrm{m}}}\frac{\partial C_a}{\partial x} + \frac{\partial^2 C_a}{\partial x^2} - \frac{Q^*}{k_B T_{\mathrm{m}}^2}\frac{j^2\rho}{k_T}C_a + \frac{Q^*}{k_B T_{\mathrm{m}}^2}\left(-\frac{j^2\rho}{k_T}x + \frac{j^2\rho L}{2k_T}\right)\frac{\partial C_a}{\partial x}\right] \tag{24}$$

For Blech structure, the above equation was solved numerically with the following initial condition and boundary conditions,

$$C_a(x,\ 0) = C_{a0} \tag{25}$$

$$J_a(0,\ t) = -\frac{\partial C_a(0,\ t)}{\partial x} + \frac{C_a(0,\ t)Z^* e\rho j}{k_B T_{\mathrm{m}}} - \frac{Q^*}{k_B T_{\mathrm{m}}^2}\frac{j^2\rho L C_a(0,\ t)}{2k_T} = 0 \tag{26}$$

$$J_a(L,\ t) = -\frac{\partial C_a(L,\ t)}{\partial x} + \frac{C_a(L,\ t)Z^* e\rho j}{k_B T_{\mathrm{m}}} - \frac{Q^*}{k_B T_{\mathrm{m}}^2}\frac{j^2\rho L C_a(L,\ t)}{2k_T} = 0 \tag{27}$$

Solving Eqs. (24) to (27), the atomic concentration C_{a} can be obtained as a function of time t and location x. Since the damage in Blech structure occurs first at the two ends, the void growth model introduced in Part I was applied as soon as C_{a} reached $C_{\mathrm{a,critical}}$ at the ends, as follows,

$$V_{\text{drift}} = \Omega L \left.\frac{\partial J_a}{\partial x}\right|_{x=0} \tag{28}$$

where

$$\left.\frac{\partial J_a}{\partial x}\right|_{x=0} = D_a \left(-\left.\frac{\partial^2 C_a}{\partial x^2}\right|_{\substack{x=0 \\ t=t(\text{failure})}} + \frac{Z^* e\rho j}{k_B T_{\text{m}}} \left.\frac{\partial C_a}{\partial x}\right|_{\substack{x=0 \\ t=t(\text{failure})}} + \frac{Q^*}{k_B T_{\text{m}}^2}\frac{j^2\rho}{2k_T} C_{\text{a,critical}} - \frac{Q^*}{k_B T_{\text{m}}^2}\frac{j^2\rho L}{2k_T}\left.\frac{\partial C_a}{\partial x}\right|_{\substack{x=0 \\ t=t(\text{failure})}} \right) \tag{29}$$

Eq. (29) was an extension to the void growth model for considering the temperature gradient as well. Thus, the void growth length at time t was

$$L_{\text{void}}(t) = [t - t(\text{failure})]\Omega L \left.\frac{\partial J_a}{\partial x}\right|_{x=0} \tag{30}$$

As a result, not only the conductor length was adjusted accordingly but also the boundary conditions at both ends were adjusted. For example, at the cathode, Eq. (26) was replaced by

$$C_a|_{x=L_{\text{void}}} = C_{\text{a,crictial}} \tag{31}$$

3.3. SWEAT structure

For the SWEAT structure, the governing equation of atomic concentration in an un-passivated conductor is the same as Eq. (24) but with the following boundary conditions,

$$C_a(0,\ t) = C_{a0} \tag{32}$$

$$C_a(L,\ t) = C_{a0} \tag{33}$$

and the initial condition is the same as Eq. (25). In Part I, we showed that C_{a} in SWEAT structure without considering TM is a constant along the entire conductor for all time, as follows

$$C_a(x,t) = C_{a0} \tag{34}$$

The new solutions based on Eqs. (24), (25), and (32)-(33) were compared to Eq. (34) in the subsequent section.

In SWEAT structures, we also developed a formulation between the resistance change and atomic concentration evolution. We assumed that the electrical resistivity changes due to C_{a} variations as the following function,

$$\frac{\rho}{\rho_0} = \frac{C_a}{C_{a0}} \rightarrow \rho = \rho_0 \frac{C_{a0}}{C_a} \tag{35}$$

where ρ is the resistivity and ρ_0 is the initial resistivity. And the initial resistance was

$$R_0 = \rho_0 AL \tag{36}$$

where A and L are the cross-section area and length of the conductor, respectively. Thus, the resistance due to atomic concentration change was

$$R(t) = \rho_0 A \int_0^L \frac{C_{a0}}{C_a(x,t)} dx \tag{37}$$

Thus, the normalized change in resistance was obtained as follows:

$$\frac{R - R_0}{R_0} = \frac{\int_0^L \frac{C_{a0}}{C_a(x,t)} dx}{L} - 1 \tag{38}$$

where the atomic concentration $C_{\text{a}}(x,t)$ was determined by solving Eqs. (24), (25), (32), and (33).

3.4. Steady-state equation

Steady-state solutions are useful to determine the threshold condition where the metal line is immune from EM failure. In a steady state, the left side of Eq. (24) became zero, and the governing equation became an ordinary differential equation as follows,

$$0 = -\frac{Z^* e\rho j}{k_B T_{\text{m}}}\frac{dC_a}{dx} + \frac{d^2 C_a}{dx^2} - \frac{Q^*}{k_B T_{\text{m}}^2}\frac{j^2\rho}{k_T} C_a + \frac{Q^*}{k_B T_{\text{m}}^2}\left(-\frac{j^2\rho}{k_T} x + \frac{j^2\rho L}{2k_T} \right)\frac{dC_a}{dx} \tag{39}$$

No analytical solution is available for Eq. (39). In the next section the numerical solutions of Eq. (39) were obtained to determine the threshold conditions for both Blech and SWEAT structures.

4. Results and discussion

Table 1 provided Al's material properties at 250 °C for obtaining numerical results based on the equations in the previous section. In this table, Q^*, the heat of transport, was introduced to account for the temperature gradient effect. The critical atomic concentration, $C_{a,critical}$, determined previously (Cui et al., 2023a), was used to determine the failure time and location.

In addition, the vacancy relaxation factor, f, as a function of atomic concentration, was calculated from molecular dynamics (MD) simulations (Cui et al., 2021), as follows.

$$f(C_a) = \begin{cases} f_0, \ 0.9925 \le \dfrac{C_a}{C_{a0}} \le 1.0025 \\ A\exp\left[B\left(1 - \dfrac{C_a}{C_{a0}}\right)\right], \ \text{else} \end{cases} \tag{40}$$

where f_0=0.73, $A = 1.08$, and B=−55.30. Additionally, using the Arrhenius equation, the temperature-dependent atomic diffusivity, D_a, was obtained as follows (Cui et al., 2022),

$$D_a = 8 \times 10^{-8}\exp\left(-\frac{0.57\ \text{eV}}{k_B T}\right)\ \text{m}^2\Big/\text{s} \tag{41}$$

4.1. Results when $j = 1$ MA/cm^2

We reported the numerical results without considering the temperature gradient in Part I under $j = 1$MA/cm^2, which agreed with the experimental observation. However, we have not verified that the results are still valid when the temperature gradient is considered. Here, using Eqs. (24-31), Fig. 8(a) and (b) showed the numerical results of normalized atomic concentrations (C_a/C_{a0}), in red color lines, at 3 h and 20 h, respectively, for an 800 μm conductor. For comparison, the results of C_a/C_{a0} without the consideration of TM were shown in blue color. The normalized critical atomic concentration $C_{a,\ critical}/C_{a0}$ was in light green color in the figures. It clearly showed that the effect of TM was negligible at 3 h and was insignificant even at 20 h. These results validated the simulation results for the Blech structures in Part I.

Furthermore, Fig. 8(c) and (d) plotted C_a/C_{a0} distribution at different time intervals for 800 μm conductor in the SWEAT structures, with and without TM, under $j = 1$MA/cm^2. When TM was taken into account, the atomic concentration did not maintain a constant value in the conductor anymore. However, the difference was only about 1%, which was still far away from $C_{a,\ critical}/C_{a0}$ at 3 h and 20 h. This implied that the constant values of C_a in SWEAT structures given in Part I provided a good approximation under $j = 1$MA/cm^2.

4.2. Effect of TM

4.2.1. Temperature and temperature gradient

The impact of TM was discussed extensively below. We first presented the results of temperature and its gradient, based on Eqs. (22) and (23), as shown in Fig. 9. Fig. 9(a) plotted the maximum temperature and temperature gradient when j increased from 1 MA/cm^2 to 5 MA/cm^2 in an 800 μm conductor. The temperature gradient squarely increased with current density, from 144 K/cm to 3600 K/cm, while the maximum temperature increased from 253 °C to 335 °C, which are well below the melting temperature. As an example, Fig. 9 (b) showed the profiles of temperature and temperature gradient under $j = 5$ MA/cm^2. The maximum temperature was at the center, but the maximum temperature gradient was at both ends in opposite directions. Moreover, Fig. 9(c) displayed the maximum temperature gradient as a function of conductor length when $j = 3$ MA/cm^2. The temperature gradient linearly increased with the conductor length. With $L = 60$, 100, and 800 μm, the maximum temperature gradient increased to 97 K/cm, 162 K/cm, and 1294 K/

Table 1
Material properties of Al used in simulations.

Property	Value
Atomic volume (Ω)	1.66×10^{-29} m^3
Electrical resistivity (ρ)	3.22×10^{-8} Ohm•m
Electric charge (e)	1.6×10^{-19}C
Charge number (Z^*)	1.1 (Blech and Herring, 1976)
Heat of transport (Q^*)	0.3 (Oriani, 1969)
Critical atomic concentration ($C_{a,critical}$)	$0.963C_{a0}$
Vacancy volume relaxation factor (f)	Eq. (40)
Atomic diffusivity (D_a)	Eq. (41)
Modified thermal conductivity (k_T)	7.5×10^4 W/(m• °C)
Thermal conductivity for Al (k_{Al})	249 W/(m• °C)

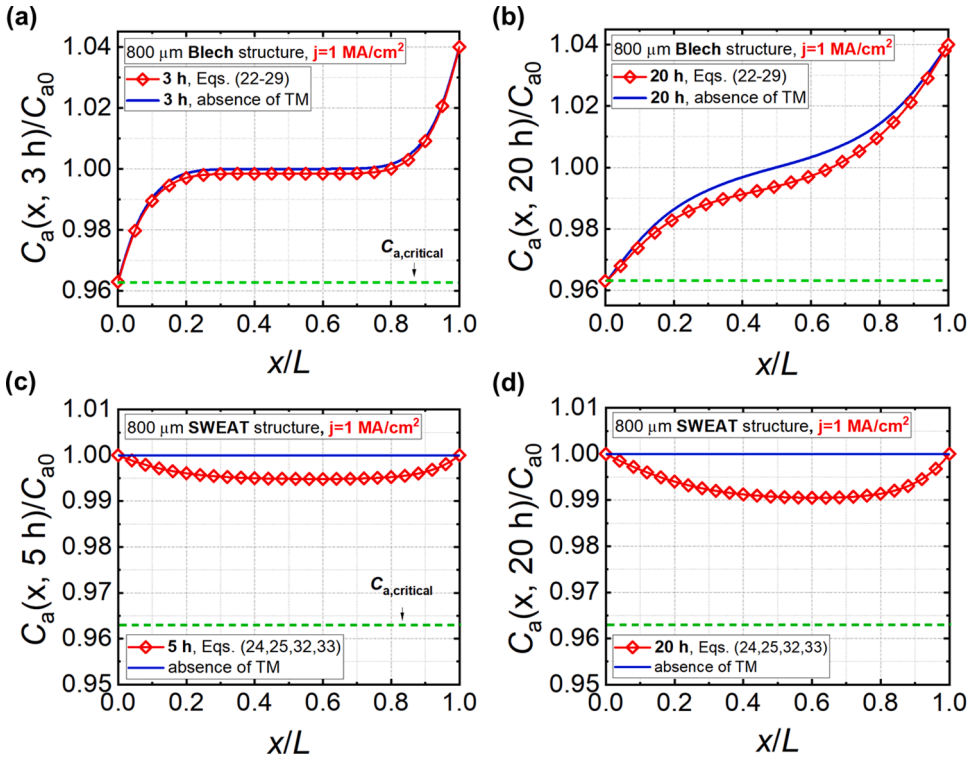

Fig. 8. Numerical results for the distribution of the normalized atomic concentration C_a/C_{a0} in 800 μm Al specimens with Blech structure under j = 1 MA/cm^2 at 3 h (a) and 20 h (b), and Al specimens with SWEAT structure under j = 1 MA/cm^2 at 5 h (c) and 20 h (d).

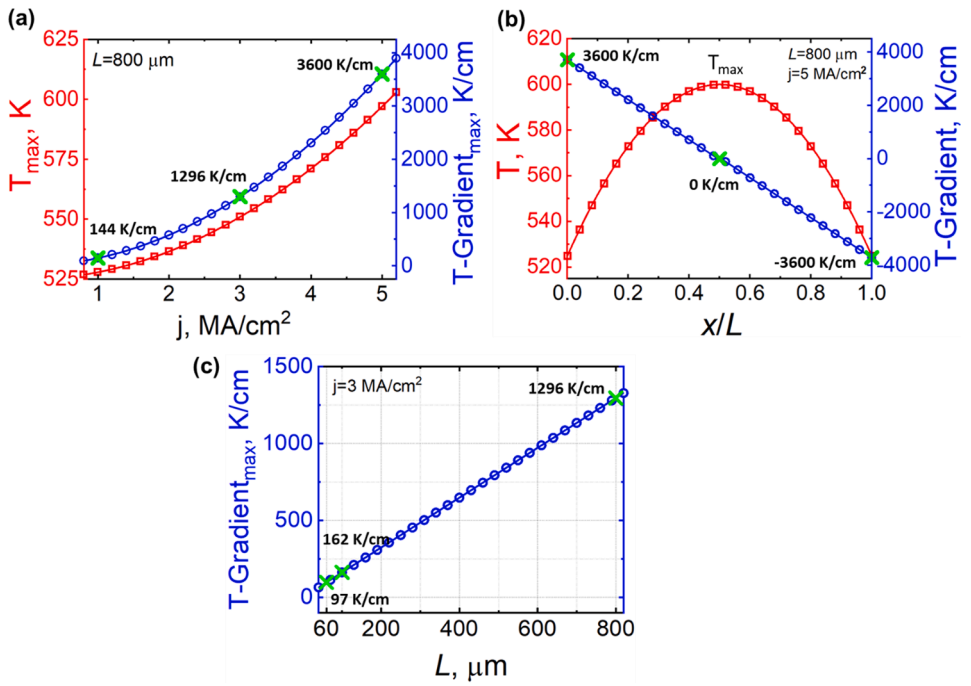

Fig. 9. (a) Maximum temperature and temperature gradient as a function of j for an 800 μm conductor. (b) Distributions of the temperature and the temperature gradient for an 800 μm conductor under j = 5 MA/cm^2. (c) Maximum temperature gradient as a function of conductor length under j = 3 MA/cm^2.

cm, respectively.

4.2.2. Blech structure

The role of TM in the Blech structures was first investigated. Fig. 10 (a-c) plotted C_a/C_{a0} distributions under $j = 3$ MA/cm^2 at 5 min, 3 h, and 15 h, respectively, for 800 μm conductors with and without considering TM. At 5 min, void and hillock were already formed at both ends. But TM's effect was negligible. However, at 3 h, TM caused a noticeable change of atomic concentration in the middle region of the conductor, despite being still well above $C_{a,\ critical}/C_{a0}$. At 15 h, C_a/C_{a0} in a broad middle of conductor reached the critical value. There was a significant time lag between the voids formed at the cathode and in the middle. With further increased $j = 5$ MA/cm^2, Fig. 10 (e-g) plotted the results of C_a/C_{a0} at 150 s, 1 h, and 4 h, respectively. At 4 h, C_a at the middle region decreased to the critical value, indicating a conductor breaking. These simulation results were in good agreement with the experimental observations shown in Section 2. TM had little effect on the initial failure at both ends but played a key role in the damage in the middle region of the conductor at a later stage.

Furthermore, Fig. 11 plotted the evolutions of C_a/C_{a0} at a fixed point in the middle ($x = 0.65\ L$) in different conductor lengths under $j = 3$ MA/cm^2. When the conductor lengths were 60 and 100 μm, the predicted C_a/C_{a0} at $x = 0.65\ L$ reached the steady state at 20 h but was still above the critical value, indicating no void formation. When the conductor length was 800 μm, C_a/C_{a0} at $x = 0.65\ L$ decreased below the critical atomic concentration at 15 h, indicating the void formation. Those predictions were consistent with the experimental observations.

4.2.3. SWEAT structure

Next, let us examine the role of TM in the SWEAT structures. For 800 μm conductors, the normalized atomic concentration C_a/C_{a0} distribution was obtained based on Eqs. (24), (25), (32), and (33) and displayed in Fig. 12. Fig. 12(a) showed that under $j = 3$ MA/cm^2, significant variation in C_a/C_{a0} was observed at 5 h and 10 h, but still well above $C_{a,\ critical}/C_{a0}$. At 16 h, C_a, at the right of the center, decreased below the critical value, indicating conductor breaking. When j increased to 5 MA/cm^2, as shown in Fig. 12(b), C_a in a broad middle region decreased below the critical value at 5 h. This implied a spread of failure in conductors. Furthermore, using Eq. (38), we calculated the change in resistance until C_a reaches $C_{a,critical}$, as plotted in Fig. 12(c) for the lengths of 800 μm under current densities of 1, 3, and 5 MA/cm^2. Simulation results agreed well with the in-situ electric resistance measurement.

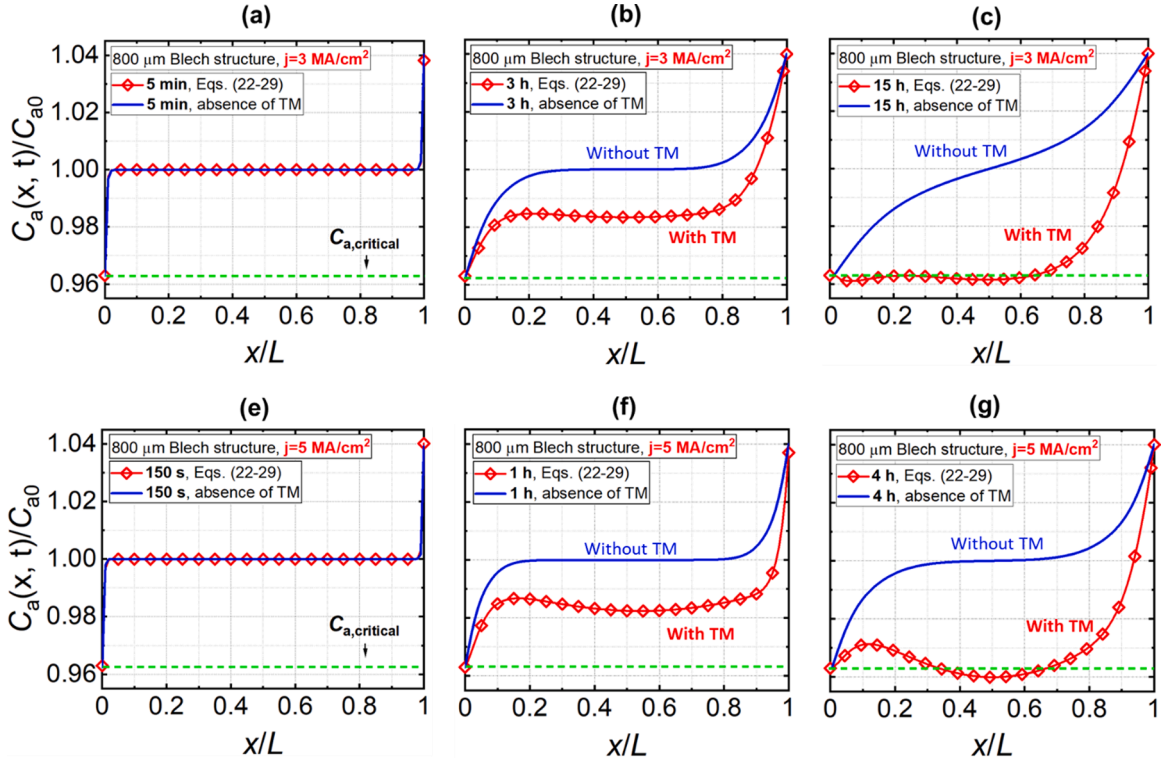

Fig. 10. Numerical results for the distribution of the normalized atomic concentration C_a/C_{a0} in 800 μm Al specimens with Blech structure under the various current densities at different times. (a), (b), and (c) for the conductor under $j = 3$ MA/cm^2 at 5 min, 3 h and 15 h, respectively. (e), (f), and (g) for the conductor under $j = 5$ MA/cm^2 at 150 s, 1 h and 4 h, respectively.

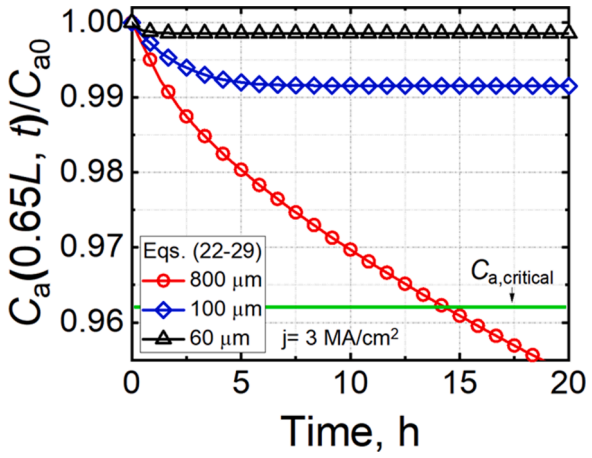

Fig. 11. Evolution of the normalized atomic concentration C_a/C_{a0} versus time at $x = 0.65$ L (a representative position in the middle region) for the Blech structure with 60/100/800 lengths.

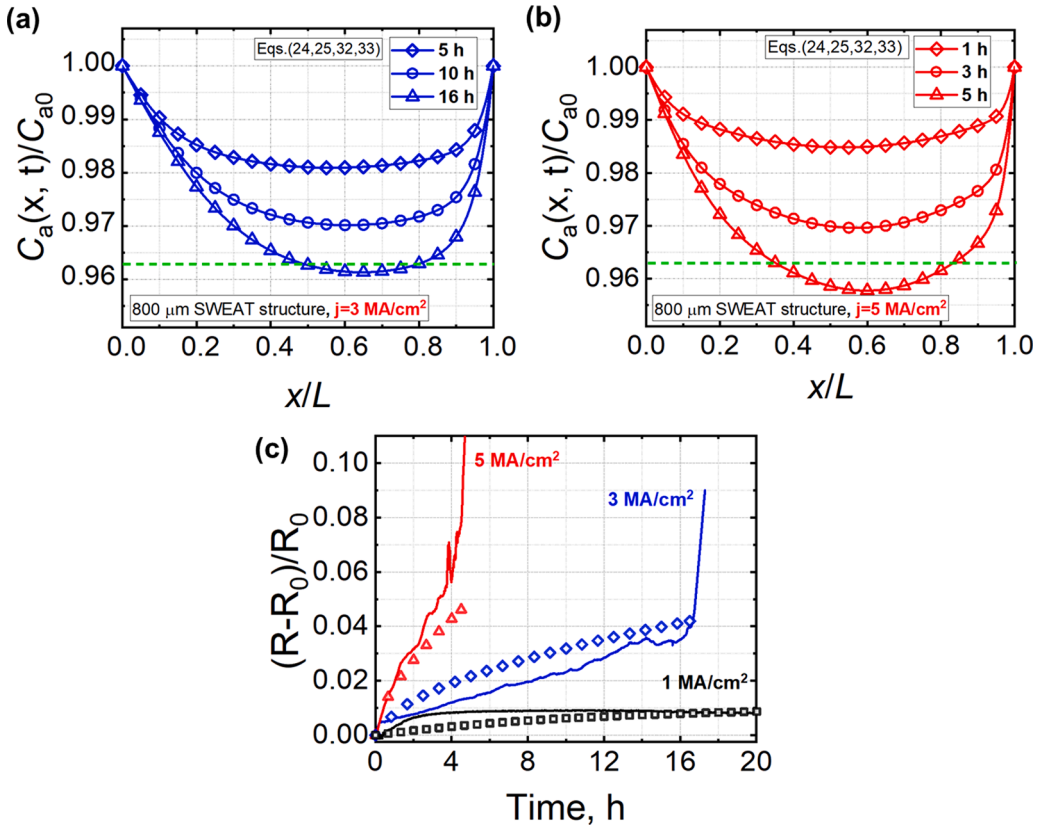

Fig. 12. Simulation results of atomic concentration distribution along the 800 μm SWEAT structure under current densities of (a) 3 MA/cm^2 and (b) 5 MA/cm^2. (c) Comparison between the electrical resistance changes from the simulation and experiment for the 800 μm SWEAT structures under different current densities. The solid lines in (c) represent measurement results, and the symbols represent the simulation results.

*4.3. Positive and negative Q**

Q^* for Al, is a positive value, as shown in Table 1, meaning that the atomic flux by TM drives the atom from the hot to the cold side. However, in Pb-free SnAg solder bumps, the Sn atoms moved to the hot end in SnAg matrix because Q^* is a negative value (Chen et al., 2012a). The direction of atomic diffusion subjected to a temperature gradient was studied using molecular dynamic (MD) simulation in the following. To simplify the problem, Al and Sn nanowires with a length of 20 nm, connected to two large cross-sections at both ends,

were constructed in our MD simulations. The simulation details and procedures were described in (Cui, 2021). Fig. 13(a) and (b) plotted the displacement of Al atoms in the z-direction and its displacement vector, respectively. The temperatures at the bottom and top were set as 900 K and 300 K, respectively. Thus, the magnitude of the temperature gradient in the nanowire was 30 K/nm. From 0 ns to 5 ns, Al atoms tended to diffuse from the hot region to the cold region. The enlarged image of the displacement vector showed that the direction of atomic motion was from the bottom to the top (from hot to cold). However, the displacement contour diagram in Fig. 13(c) indicated that most of the Sn atoms in the nanowire moved from the cold region to the hot region. The displacement vector in Fig. 13(d) also showed that the Sn atoms tended to diffuse downward from cold to hot. This indicated that we can use MD simulation to predict the sign of Q^*.

4.4. Threshold conditions

Without considering TM in Part I (Cui et al., 2023a), we have determined the critical products of current density and conductor length for un-passivated and passivated Al lines. Such threshold conditions in un-passivated configuration, without TM, were expressed as follows,

$$jL = (jL)_c = \begin{cases} 1000\ A/m, & \text{Blech structure} \\ \\ \infty, & \text{SWEAT structure} \end{cases} \tag{42}$$

where an infinity value in the SWEAT structures means no EM damage would occur in the SWEAT structures with current density in any length in the absence of TM.

When TM was considered, however, no analytical solutions were available from Eq. (19) or (39) with the corresponding boundary conditions in both Blech and SWEAT structures. But we were still able to solve the equations numerically to obtain the threshold

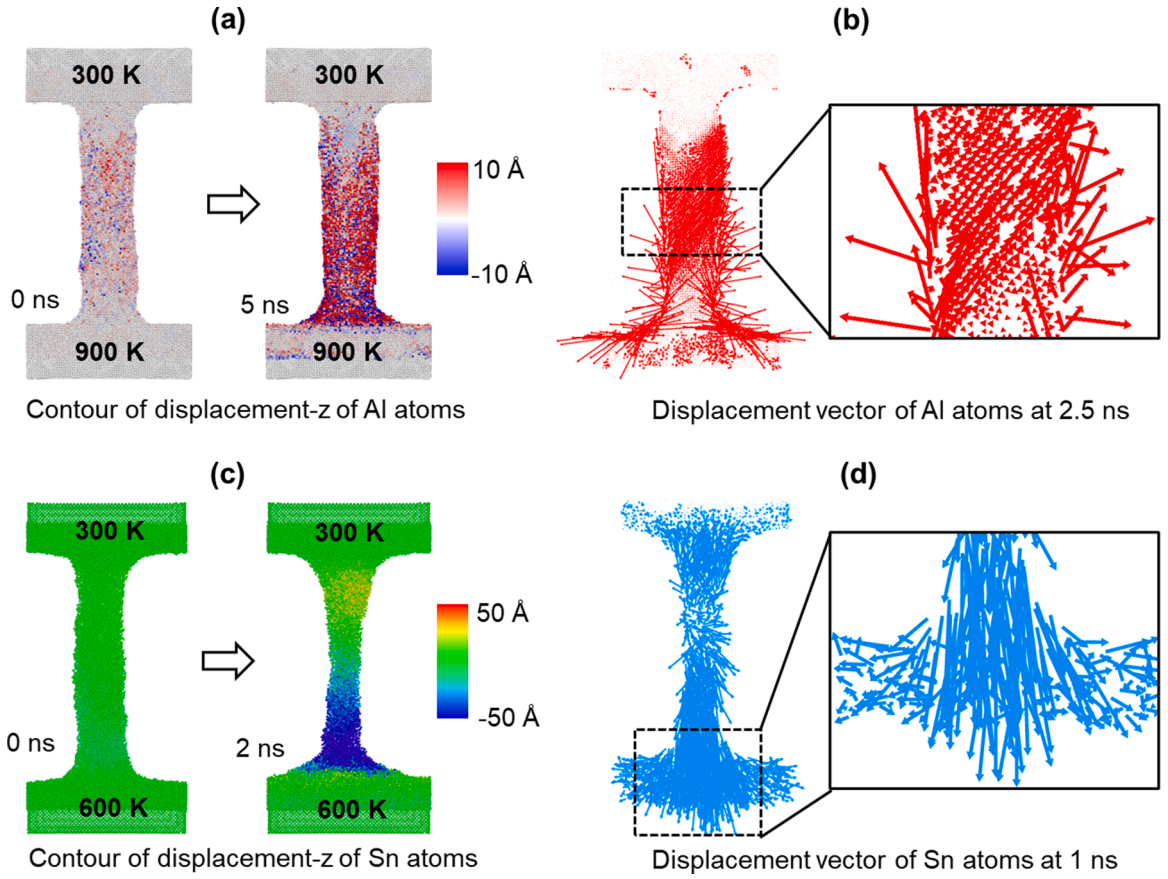

Fig. 13. MD simulation results for the motions of Al and Sn atoms under temperature gradients. (a) Contour of displacement in z-direction for Al atoms at 0 ns and 5 ns. (b) Displacement vector of Al atoms in the unit of Å after 2.5 ns MD simulation. (c) Contour of displacement in z-direction for Sn atoms at 0 ns and 2 ns. (d) Displacement vector of Sn atoms in the unit of Å after 1 ns MD simulation. The red and blue arrows in zoom-in figures indicate the atoms moving upward and downward. MD results were visualized using OVITO (Stukowski, 2009).

conditions. Fig. 14 displayed the numerical results of the threshold curves in Blech and SWEAT structures in the range of current density from 0.5 MA/cm^2 to 8 MA/cm^2. After curve fitting, the new threshold conditions in un-passivated configuration considering TM, were approximately expressed as follows,

$$\begin{cases} jL = (jL)_c = 1000\ A/m, & \text{Blech structure} \\ jL^2 = (jL^2)_c = 15300\ A, & \text{SWEAT structure} \end{cases} \tag{43}$$

For Blech structures, the threshold condition was exactly the same as Eq. (42) without TM. This means that TM does not affect the threshold condition of EM failure in the Blech structures because the initial failure always occurred at the ends, on which TM had a negligible impact. For the SWEAT structure, however, we found the threshold condition in the form of the product of the current density and the square of critical length (jL^2), as shown in Eq. (43). From Fig. 14, the SWEAT structures can tolerate larger current densities than Blech structures without failures. The threshold conditions shown in Eq. (43) included the effects of TM and self-diffusion. Therefore, the threshold conditions in Eq. (43) are major extensions to the original Blech's threohold condition, in which only the mechanical stress gradient was considered.

4.5. Current density exponent n

We investigated the current density exponent n for un-passivated and passivated configurations in Part I without considering TM. We discovered that in a certain range of current density, the failure time due to EM follows Black's law with the exponent of 2 when Blech structure is used. However, in a low level of current density, the exponent increases rapidly from 2 to infinity as this level of current density falls into the zone immune from EM failure. When SWEAT structures were used, no EM damage would occur without taking TM into consideration.

Now let us investigate the impact of TM on the exponent n. As an illustration, an 800 μm length conductor was considered in both Blech and SWEAT structures. Fig. 15 plotted time to failure versus j ranging from 0.1 MA/cm^2 to 5 MA/cm^2 for both Blech and SWEAT structures. In Blech structures, a curve-fitting showed that when the current density ranged from 0.2 – 5 MA/cm^2, the exponent followed approximately as $n = 2$, indicating TM's effect was negligible. When j further decreased, the exponent n increased rapidly to infinity as it entered the immune zone. On the other hand, in SWEAT structures, a curve-fitting showed that when the current density ranged from 2.1 – 5 MA/cm^2, the exponent followed approximately as $n = 4.2$. When j further decreased, the exponent n increased rapidly to infinity as it entered the immune zone.

5. Conclusions

With a high electrical current applied to a microelectronic device, temperature gradients, which are generated owing to Joule heating, induce thermomigration. EM, TM, self-diffusion and stress migration are coupled with each other. In this paper, based on the coupled 3D theory developed in Part I, the new 1D analytical solutions in terms of atomic concentration were obtianed with considering TM. We first verified that temperature gradient could be neglected under a low level of current density. At elevated current densities, however, TM significantly affected EM performance.

In the Blech structures, voids in the middle region of conductors were observed after a period of time when voids/hillocks were formed and grown at both ends. Through experiments and simulations, we found the following.

1 Temperature gradient played a significant role in the EM development in the middle of conductors. There was a significant time delay between the failure at both ends and in the middle. Moreover, a broad region in the middle of the conductors displayed a decrease in atomic concentration, indicating the spread of voids in the conductors. The simulation results agreed well with the experimental observations.
2 Despite TM's impact on the damage in the middle of conductors, TM had a negligible effect on failures at two ends, which occurred first, even at the elevated current densities. In other words, the models developed in Part I without considering TM are still valid in determining the time to failure at the ends. Consequently, the critical threshold product for current density and conductor length, derived from Part I, without considering TM, provided almost identical results to those with consideration of TM.
3 The exponent of current density, described in Black's law, maintained a value of 2 in the range of the current density from 0.2 to 5 MA/cm^2. The exponent then rapidly increased and approached infinity if the current density fell below the critical current density. Such conclusions are the same with or without considering TM.

On the other hand, in the SWEAT structures, with further increasing current density, voids spread over the conductors and broke in the right of the center when the current flowed from left to right. Through experiments and simulations, we found the following.

1 When TM was taken into consideration, atomic concentration in the middle region of the conductors decreased over time. A broad region in the middle of the conductors displayed a decrease in atomic concentration, indicating the spread of voids in the conductors. Different from the Blech structures, no failures occurred at the two ends in the SWEAT structures. The simulation results agreed well with the experimental observations.

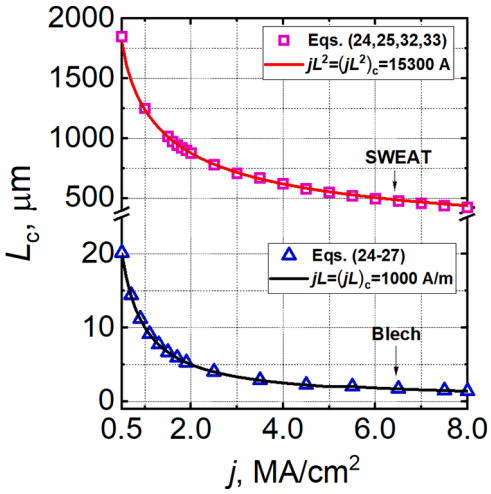

Fig. 14. Critical length for conductors with Blech and SWEAT structures under current densities from 0.5 MA/cm^2 to 8 MA/cm^2. Square and triangle symbols represent the numerical results for SWEAT and Blech structures, respectively. The solid line for Blech structure is the result of $jL = (jL)_c = 1000$ A/m. The solid line for the SWEAT structure is the result of $jL^2 = (jL^2)c = 15{,}300$ A.

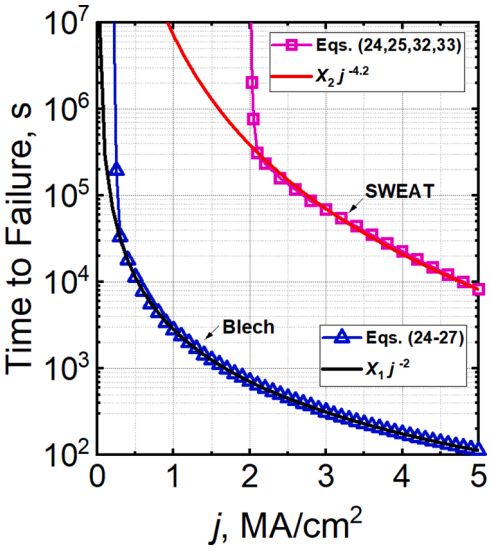

Fig. 15. Predictions of the current density exponent n for time to failure. Square and triangle symbols represented the numerical results for SWEAT and Blech structures, respectively. The black line was the results of $t_f = X_1 j^{-2}$ with $X_1 = 2823$ s•MA/cm^2, and the red line was the result of $t_f = X_2 j^{-4.2}$ with $X_2 = 7.08 \times 10^6$ s•MA/cm^2.

2 The critical threshold condition considering TM was in the form of the product for current density and the square of conductor length. A higher level of current density is required to induce failure in SWEAT structures, compared to the same length in Blech structures.
3 The exponent of current density fits a value of 4.2 in the range of the current density from 2 to 5 MA/cm^2. The exponent then rapidly increases and approaches infinity if the current density falls below the critical current density. The critical current density in the SWEAT structures is higher than that in the Blech structures.

It is worth noting that the above conclusions were based on the temperature profiles using Eq. (20). Accurate temperature and temperature gradient can be obtained based on numerical analysis (Cui et al., 2023b). Additionally, in the above analysis, we considered the conductor's self-Joule heating without externally applied temperature gradient. If a conductor line is subjected to an external temperature gradient due to external Joule heating, the temperature gradient may become an independent factor affecting EM development. The threshold conditions for EM failure could be much more complicated among three parameters: current density, conductor length, and temperature gradient. Additionally, the sign of Q^*, which determines the motion direction of the atomic flux by the temperature gradient, can be determined using MD simulation.

When a passivated configuration is considered, we need to further extend the theory to evaluate the effect of mechanical stress and mechanical stress gradient in the presence of temperature gradient. We will report our results in the future. Additionally, with a 3D theory in place, we will study the effect of current crowding and the impact of temperature gradient externally exerted on EM development.

CRediT authorship contribution statement

Zhen Cui: Methodology, Software, Investigation, Formal analysis, Validation, Visualization, Writing – original draft. **Xuejun Fan:** Conceptualization, Methodology, Investigation, Formal analysis, Supervision, Validation, Visualization, Writing – original draft. **Yaqian Zhang:** Methodology, Investigation. **Sten Vollebregt:** Methodology, Validation, Supervision, Writing – review & editing. **Jiajie Fan:** Writing – review & editing. **Guoqi Zhang:** Supervision, Resources, Writing – review & editing.

Declaration of Competing Interest

The authors declare that they have no known competing financial interests or personal relationships that could have appeared to influence the work reported in this paper.

Data availability

Data will be made available on request.

Acknowledgments

The authors would like to thank the staff of the Else Kooi Laboratory for processing support. Xuejun Fan would like to acknowledge the support from Lamar University and Delft University of Technology (TU Delft) during his sabbatical leave at TU Delft. He also would like to acknowledge his former doctoral student, Dr. Kasemsak Kijkanjanapaiboon, for his dedication and diligence during his doctoral study of this topic.

References

Abdulhamid, M.F., Basaran, C., Lai, Y.-S., 2009. Thermomigration versus electromigration in microelectronics solder joints. IEEE Trans. Adv. Packag. 32, 627–635.
Berenbaum, L., 1971. Electromigration damage of grain-boundary triple points in Al thin films. J. Appl. Phys. 42, 880–882.
Blech, I., Herring, C., 1976. Stress generation by electromigration. Appl. Phys. Lett. 29, 131–133.
Blech, I., Meieran, E., 1969. Electromigration in thin Al films. J. Appl. Phys. 40, 485–491.
Blech, I., Tai, K., 1977. Measurement of stress gradients generated by electromigration. Appl. Phys. Lett. 30, 387–389.
Blech, I.A., 1976. Electromigration in thin aluminum films on titanium nitride. J. Appl. Phys. 47, 1203–1208.
Cahn, R.W., Haasen, P., 1996. Physical Metallurgy. Elsevier.
Ceric, H., de Orio, R.L., Cervenka, J., Selberherr, S., 2008. A comprehensive TCAD approach for assessing electromigration reliability of modern interconnects. IEEE Trans. Device Mater. Reliab. 9, 9–19.
Ceric, H., Heinzl, R., Hollauer, C., Grasser, T., Selberherr, S., 2006. Microstructure and stress aspects of electromigration modeling. In: AIP Conference Proceedings. American Institute of Physics, pp. 262–268.
Chen, C., Hsiao, H.-Y., Chang, Y.-W., Ouyang, F., Tu, K.-N., 2012a. Thermomigration in solder joints. Mater. Sci. Eng.: R: Rep. 73, 85–100.
Chen, C., Hsiao, H.-Y., Chang, Y.-W., Ouyang, F., Tu, K.-N., 2012b. Thermomigration in solder joints. Mater. Sci. Eng.: R: Rep. 73, 85–100.
Chen, C., Tong, H., Tu, K.-N., 2010. Electromigration and thermomigration in Pb-free flip-chip solder joints. Annu. Rev. Mater. Res. 40, 531–555.
Chen, H.-Y., Chen, C., Tu, K.-N., 2008. Failure induced by thermomigration of interstitial Cu in Pb-free flip chip solder joints. Appl. Phys. Lett. 93, 122103.
Chen, H.-Y., Lin, H.-W., Liu, C.-M., Chang, Y.-W., Huang, A.T., Chen, C., 2012c. Thermomigration of Ti in flip-chip solder joints. Scr. Mater. 66, 694–697.
Christou, A., 1973. Electro-thermomigration in Al/Si, Au/Si interdigitized test structures. J. Appl. Phys. 44, 2975–2979.
Zhang, Y., Liu, Y., Liang, L., Fan, X., 2012. The effect of atomic density gradient in electromigration. Int. J. Mater. Struct. Integr. 6, 36–53.
Cui, Z., 2021. Multi-Physics Driven Electromigration Study: Multi-Scale Modeling and Experiment, Ph.D. Dissertation. Delft University of Technology.
Cui, Z., Fan, X., Zhang, G., 2019. General coupling model for electromigration and one-dimensional numerical solutions. J. Appl. Phys. 125, 105101.
Cui, Z., Fan, X., Zhang, G., 2020. Implementation of general coupling model of electromigration in ANSYS. In: 2020 IEEE 70th Electronic Components and Technology Conference (ECTC). IEEE, pp. 1632–1637.
Cui, Z., Fan, X., Zhang, G., 2021. Molecular dynamic study for concentration-dependent volume relaxation of vacancy. Microelectron. Reliab. 120, 114127.
Cui, Z., Fan, X., Zhang, Y., Vollebregt, S.F., Jiajie, Zhang, G., 2023a. Coupling Model of Electromigration and Experimental Verification – Part I: effect of Atomic Concentration Gradient. Preceding paper.
Cui, Z., Fan, X., Zhang, Y., 2023b. Effect of thermomigration on electromigration. In: SWEAT structures. 24th International Conference on Thermal, Mechanical and Multi-Physics Simulation and Experiments in Microelectronics and Microsystems, Graz, Austria.
Cui, Z., Zhang, Y., Hu, D., Vollebregt, S., Fan, J., Fan, X., Zhang, G., 2022. Effects of temperature and grain size on diffusivity of aluminium: electromigration experiment and molecular dynamic simulation. J. Phys. Condens. Matter 34, 175401.
d'Heurle, F.M., 1971. Electromigration and failure in electronics: an introduction. Proc. IEEE 59, 1409–1418.
Dandu, P., Fan, X., 2011. Assessment of current density singularity in electromigration of solder bumps. IEEE, pp. 2192–2196.
Giroux, F., Gounelle, C., Mortini, P., Ghibaudo, G., 1995. Wafer-level electromigration tests on NIST and SWEAT structures. In: Proceedings International Conference on Microelectronic Test Structures. IEEE, pp. 229–232.
Giroux, F., Gounelle, C., Vialle, N., Mortini, P., Ghibaudo, G., 1994. Current and temperature distribution impact on electromigration failure location in SWEAT structure. In: Proceedings of 1994 IEEE International Conference on Microelectronic Test Structures. IEEE, pp. 214–217.
He, J., Suo, Z., Marieb, T., Maiz, J., 2004. Electromigration lifetime and critical void volume. Appl. Phys. Lett. 85, 4639–4641.
Hemmert, R., Costa, M., 1991. Electromigration-induced compressive stresses in encapsulated thin-film conductors. IEEE Proc. Int. Reliab. Phys. Symp 64–69.
Hsiao, H.-Y., Chen, C., 2009. Thermomigration in Pb-free SnAg solder joint under alternating current stressing. Appl. Phys. Lett. 94, 092107.
Hu, C.-K., Luther, B., 1995. Electromigration in two-level interconnects of Cu and Al alloys. Mater. Chem. Phys. 41, 1–7.

Hu, C.K., Ho, P., Small, M., 1992. Electromigration in two-level interconnect structures with Al alloy lines and W studs. J. Appl. Phys. 72, 291–293.
Hu, C.K., Small, M., Ho, P., 1993. Electromigration in Al (Cu) two-level structures: effect of Cu and kinetics of damage formation. J. Appl. Phys. 74, 969–978.
Huang, A.T., Tu, K.-N., Lai, Y.-S., 2006. Effect of the combination of electromigration and thermomigration on phase migration and partial melting in flip chip composite SnPb solder joints. J. Appl. Phys. 100, 033512.
Jeong, W., Kim, K., Kim, Y., Lee, W., Reddy, P., 2014. Characterization of nanoscale temperature fields during electromigration of nanowires. Sci. Rep. 4, 1–6.
Kijkanjanapaiboon, K., 2017. Modeling of Electromigration and Lock-In Thermography in Microelectronics and Microelectronics Packaging. Ph.D Dissertation. Lamar University.
Kirchheim, R., 1992. Stress and electromigration in Al-lines of integrated circuits. Acta Metall. Mater. 40, 309–323.
Korhonen, M., Bo/rgesen, P., Tu, K.-N., Li, C.Y., 1993. Stress evolution due to electromigration in confined metal lines. J. Appl. Phys. 73, 3790–3799.
Kozlova, T., Rudneva, M., Zandbergen, H.W., 2013. situ TEM and STEM studies of reversible electromigration in thin palladium–platinum bridges. Nanotechnology 24, 505708.
Kraft, O., Arzt, E., 1998. Current density and line width effects in electromigration: a new damage-based lifetime model. Acta Mater. 46, 3733–3743.
Kraft, O., Sanchez, J., Bauer, M., Arzt, E., 1997. Quantitative analysis of electromigration damage in Al-based conductor lines. J. Mater. Res. 12, 2027–2037.
Lee, K., Hu, C., Tu, K.-N., 1995. In situ scanning electron microscope comparison studies on electromigration of Cu and Cu (Sn) alloys for advanced chip interconnects. J. Appl. Phys. 78, 4428–4437.
Lee, T.C., Tibel, D., Sullivan, T.D., Forhan, S., 2001. Comparison of isothermal, constant current and SWEAT wafer level EM testing methods. In: 2001 IEEE International Reliability Physics Symposium Proceedings. 39th Annual (Cat. No. 00CH37167. IEEE, pp. 172–183.
Liang, C.-L., Lin, Y.-S., Kao, C.-L., Tarng, D., Wang, S.-B., Hung, Y.-C., Lin, G.-T., Lin, K.-L., 2020a. Athermal and thermal coupling electromigration effects on the microstructure and failure mechanism in advanced fine-pitch Cu interconnects under extremely high current density. Mater. Chem. Phys. 256, 123680.
Liang, C.-L., Lin, Y.-S., Kao, C.-L., Tarng, D., Wang, S.-B., Hung, Y.-C., Lin, G.-T., Lin, K.-L., 2020b. Electromigration reliability of advanced high-density fan-out packaging with fine-pitch 2-/2-μm L/S Cu redistribution lines. IEEE Transact. Compon. Packag. Manufact. Technol. 10, 1438–1445.
Liu, P., 2017. Fundamentals of Electromigration in Interconnects of 3D Packaging, 3D Microelectronic Packaging. Springer, pp. 223–244.
Lloyd, J., 1999. Electromigration and mechanical stress. Microelectron. Eng. 49, 51–64.
Ludwig, C., 1856. Sitzungsberichte der Kaiserlichen Akademie der Wissenschaften. Mathematisch-Naturwissenschaftliche Klasse 20, 539.
Meechan, C., Lehman, G.W., 1962. Diffusion of Au and Cu in a temperature gradient. J. Appl. Phys. 33, 634–641.
Nucci, J., Straub, A., Bischoff, E., Arzt, E., Volkert, C., 2002. Growth of electromigration-induced hillocks in Al interconnects. J. Mater. Res. 17, 2727–2735.
Oriani, R., 1969. Thermomigration in solid metals. J. Phys. Chem. Solids 30, 339–351.
Piazza, R., Guarino, A., 2002. Soret effect in interacting micellar solutions. Phys. Rev. Lett. 88, 208302.
Platten, J.K., 2006. The Soret effect: a review of recent experimental results. J. Appl. Mech. 73, 5–15.
Proost, J., Delaey, L., D'Haen, J., Maex, K., 2002. Plasticity of electromigration-induced hillocking and its effect on the critical length. J. Appl. Phys. 91, 9108–9115.
Proost, J., Maex, K., Delaey, L., 1998. Electromigration threshold in damascene versus plasma-etched interconnects. Appl. Phys. Lett. 73, 2748–2750.
Rahman, M., Saghir, M., 2014. Thermodiffusion or Soret effect: historical review. Int. J. Heat Mass Transf. 73, 693–705.
Ross, C., Drewery, J., Somekh, R., Evetts, J., 1989. The effect of anodization on the electromigration drift velocity in aluminum films. J. Appl. Phys. 66, 2349–2355.
Sarychev, M., Zhitnikov, Y.V., Borucki, L., Liu, C.-L., Makhviladze, T., 1999. General model for mechanical stress evolution during electromigration. J. Appl. Phys. 86, 3068–3075.
Schafft, H.A., Staton, T.C., Mandel, J., Shott, J.D., 1987. Reproducibility of electromigration measurements. IEEE Trans. Electron Devices 34, 673–681.
Shen, F.-C., Huang, C.-Y., Lo, H.-Y., Hsu, W.-Y., Wang, C.-H., Chen, C., Wu, W.-W., 2021. Atomic-scale investigation of electromigration with different directions of electron flow into high-density nanotwinned copper through in situ HRTEM. Acta Mater. 219, 117250.
Shen, Y.-A., Zhou, S., Li, J., Tu, K.-N., Nishikawa, H., 2019. Thermomigration induced microstructure and property changes in Sn-58Bi solders. Mater. Des. 166, 107619.
Somaiah, N., Kumar, P., 2018. Inverse Blech Length Phenomenon in Thin-Film Stripes. Phys. Rev. Appl. 10, 054052.
Stahlmecke, B., Dumpich, G., 2007. Resistance behaviour and morphological changes during electromigration in gold wires. J. Phys. Condens. Matter 19, 046210.
Stukowski, A., 2009. Visualization and analysis of atomistic simulation data with OVITO–the Open Visualization Tool. Modell. Simul. Mater. Sci. Eng. 18, 015012.
Sukharev, V., Zschech, E., 2004. A model for electromigration-induced degradation mechanisms in dual-inlaid copper interconnects: effect of interface bonding strength. J. Appl. Phys. 96, 6337–6343.
Sukharev, V., Zschech, E., Nix, W.D., 2007. A model for electromigration-induced degradation mechanisms in dual-inlaid copper interconnects: effect of microstructure. J. Appl. Phys. 102, 053505.
Swalin, R., Yin, C., 1967. Thermal diffusion of vacancies in aluminum. Acta Metall. 15, 245–248.
Tan, C.M., Roy, A., 2007. Electromigration in ULSI interconnects. Mater. Sci. Eng.: R: Rep. 58, 1–75.
Tu, K.-N., 2003. Recent advances on electromigration in very-large-scale-integration of interconnects. J. Appl. Phys. 94, 5451–5473.
Tu, K.-N., Liu, Y., Li, M., 2017. Effect of Joule heating and current crowding on electromigration in mobile technology. Appl. Phys. Rev. 4, 011101.
Van Gurp, G., De Waard, P., Du Chatenier, F., 1985. Thermomigration in indium and indium alloy films. J. Appl. Phys. 58, 728–735.
Yao, W., Basaran, C., 2013. Computational damage mechanics of electromigration and thermomigration. J. Appl. Phys. 114, 103708.
Ye, H., Basaran, C., Hopkins, D., 2003. Thermomigration in Pb–Sn solder joints under joule heating during electric current stressing. Appl. Phys. Lett. 82, 1045–1047.